

Weierstraß-Institut

für Angewandte Analysis und Stochastik

im Forschungsverbund Berlin e. V.

Preprint

ISSN 0946 – 8633

Mode transitions in DBR semiconductor lasers: experiments, mode analysis and simulations

Mindaugas Radziunas¹, Karl-Heinz Hasler², Bernd Sumpf²,

Tran Quoc Tien^{2,3}, Hans Wenzel²

submitted: 19th May 2010

¹ Weierstrass Institute
for Applied Analysis and Stochastics
Mohrenstr. 39
10117 Berlin
Germany
E-Mail: radziuna@wias-berlin.de

² Ferdinand-Braun-Institut,
Leibniz-Institut für Höchstfrequenztechnik
Gustav-Kirchhoff-Str. 4,
12489 Berlin,
Germany
E-Mail: hasler@fbh-berlin.de
bernd.sumpf@fbh-berlin.de
wenzel@fbh-berlin.de

³ Institute of Materials Science,
Vietnamese Academy of Science and Technology,
18 Hoang Quoc Viet, Cau Giay, Hanoi,
Vietnam
E-Mail: tientq@ims.vast.ac.vn

No. 1513
Berlin 2010



2000 *Mathematics Subject Classification.* 78A60, 35Q60, 35B30, 78-05.

Key words and phrases. DBR laser, traveling wave model, thermal detuning, optical modes, mode transitions, analysis.

2010 *Physics and Astronomy Classification Scheme.* 42.55.Px, 42.65.bc, 42.60.Pk, 42.60.Mi.

Edited by
Weierstraß-Institut für Angewandte Analysis und Stochastik (WIAS)
Mohrenstraße 39
10117 Berlin
Germany

Fax: +49 30 2044975
E-Mail: preprint@wias-berlin.de
World Wide Web: <http://www.wias-berlin.de/>

Abstract

The performance of a multisection DBR semiconductor laser emitting around $1.06 \mu\text{m}$ is experimentally and theoretically investigated. Simulations and mode analysis of the traveling wave model including temperature induced changes of the refractive index explain experimentally observed nearly-periodic transitions between neighboring cavity mode determined continuous wave states with increasing injection current.

1 Introduction

Wavelength stabilized semiconductor lasers are required for many applications such as frequency conversion, free-space communication, spectroscopy and metrology. One possibility to achieve wavelength stabilization is the integration of a Bragg grating into the semiconductor chip. The resulting distributed feedback (DFB) or distributed Bragg reflector (DBR) lasers emitting several hundreds of milliwatts are ideally suited for the above mentioned applications [1, 2].

DFB lasers are typically single-section devices with the Bragg grating extending over the whole amplifying cavity. In order to facilitate an operation in the same longitudinal mode over a large power range at least the front facet is anti-reflection coated to suppress side modes. However, this leads to a high sensitivity to feedback from external surfaces and still does not exclude possible transitions between the two DFB resonance modes.

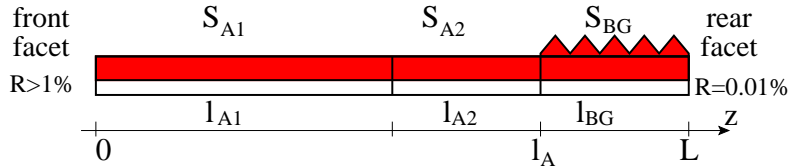


Figure 1: Scheme of a DBR semiconductor laser consisting of two amplifying sections S_{A1} , S_{A2} and DBR section S_{BG} .

DBR lasers consists of a reflector section containing the Bragg grating and one or several amplifying sections: see Fig. 1 showing a scheme of a DBR laser. In order to form a resonator, the front facets have reflectivities of $R \geq 1\%$ depending on the length of the amplifying sections. Due to the fact that all sections are differently operated, DBR lasers exhibit periodic undulations in the power-current characteristics and temporal instabilities owing to longitudinal mode hopping. On the other hand, compared to DFB lasers they are more robust to external perturbations and can be more cost-effective fabricated due to the utilization of surface Bragg gratings [3–5]. Therefore, it is of great practical interest to reduce the instability regions which often hinder the applicability of DBR lasers.

The main aim of our paper is a theoretical analysis of the mode-hopping phenomena in DBR lasers, what allows to gain more insight into the underlying physics. Our mathematical model is given by the traveling wave (TW) equations for the complex slowly varying amplitudes of the counter-propagating optical fields, coupled to equations for the induced polarization functions and the excess carrier density [6]. Following [7, 8], we relate the mode-hopping in DBR lasers with temperature induced shifts of the DBR stopband and of full cavity resonances. In the considered TW model, these thermal effects are represented by a linear nonlocal dependence of the refractive index on the inhomogeneous injection current [9].

Our explanation of the mode transitions is based on observations and analysis of *instantaneous* longitudinal optical modes [10] and their dynamics in edge-emitting multisection lasers [9, 11, 12]. According to our inhomogeneous heating model, the injection currents differently affect the refractive indices of separate laser parts and thereby tune the relative phases of the optical modes at the interface of the amplifying and reflector sections. This phase tuning is responsible for the transitions between modes, observable both in optical experiments and in simulations.

Our paper is organized as follows. In Section 2 we give a short description of the laser device and present some measured characteristics. After introducing the mathematical model in Section 3, we give a definition of optical modes, analyze relations between them and their dependence on model parameters in Section 4. Section 5 is devoted to the discussion of numerical simulation results. Finally, some conclusions are drawn in Section 6.

2 Experiments

The DBR lasers under investigation consist of 2 mm and 1 mm long amplifying sections S_{A1} , S_{A2} and a 1 mm long DBR section S_{BG} (see Fig. 1). The sixth order Bragg grating with a period of about $1 \mu\text{m}$ was defined by an i-line wafer stepper and dry etched into the surface of epitaxial layer structure [3]. The effective reflection coefficient of the Bragg grating is about 55%. The front and rear facets were coated with dielectric layers to obtain reflectivities of 1% and $\approx 0.01\%$, respectively. Fundamental lateral mode operation is ensured by a $5 \mu\text{m}$ wide ridge waveguide. The active region is a triple quantum well embedded non-centric in a super large optical cavity. More details can be found in [13].

Throughout this paper, both amplifying sections are shortened so that identical current densities are injected. Experimental characteristics of the DBR laser driven in continuous-wave mode are presented in Figs. 2 and 3. All these figures indicate nearly-periodic changes of lasing states with increase of the total current I_A injected into the amplifying sections. Fig. 2 shows the emitted optical power at the front and rear facets versus I_A . The threshold current is 90 mA. At the front facet the power-current characteristic is nearly linear with a slope efficiency of 0.75 W/A up to the power of 600 mW, except at periodically reappearing jumps.

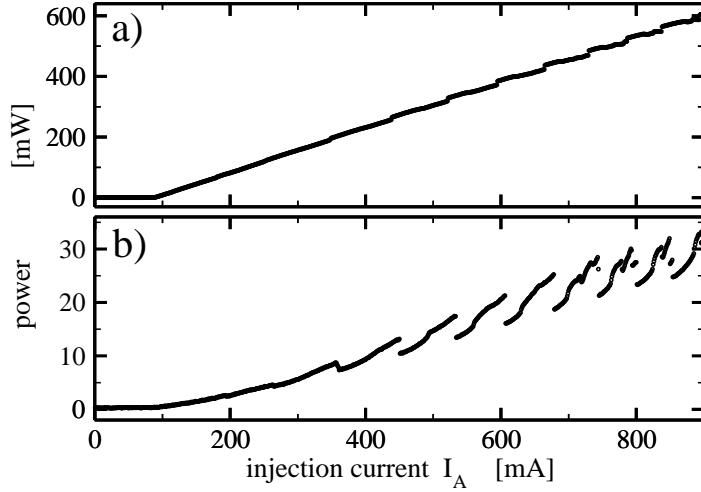


Figure 2: Power-current characteristics of the DBR laser measured at the front (a) and rear (b) facets.

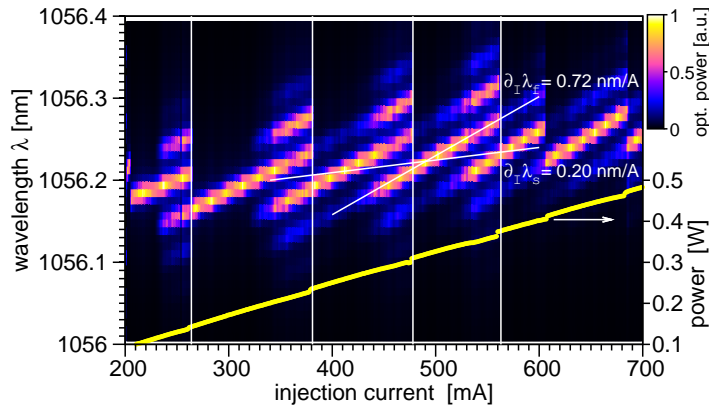


Figure 3: Representation of the measured optical spectra (mapping) and the emitted power (light curve) at the front facet of the laser as a function of the increased injection current. White slanted lines indicate the estimated slow ($\partial_I \lambda_s$) and fast ($\partial_I \lambda_f$) red shifts of the lasing wavelength, compare Eqs. (6) and (8).

We note, that while during these jumps the power emitted at the front facet increases (panel a), the power emitted at the rear facet decreases (panel b). A non-smooth increase of the power before each jump (best visible at the rear facet of the device) can be explained by a non-stationary laser emission.

This non-stationary lasing involving two or more optical modes can be also recognized in Fig. 3 where an evolution of the optical spectrum with the increase of I_A is shown. Here, each injection current “period” determined by a pair of neighboring vertical white lines contains the following typical operation regimes.

- At the left part of each period the laser shows a single wavelength emission.
- With an increase of I_A several neighboring spectral peaks start to grow indicating the formation of periodic field intensity pulsations [11].
- At the right side of each period an abrupt change of the spectrum and field intensities occur.

- After such a jump the laser shows again a single wavelength operation at the *neighboring* blue optical mode.

The step-like red shift of the spectral peaks within each period is due to a limited spectral resolution of our measuring equipment. A ~ 45 pm separation of the neighboring spectral peaks corresponds to the field round-trip time in the laser cavity, i.e., to the separation of the neighboring laser modes. The periodicity of the mode jumps, the averaged slow and periodic fast red shifts of the lasing wavelength (indicated by the slanted white lines in Fig. 3) as well as an increase or decrease of the field emission from both laser facets during the mode jumps will be discussed below in this paper.

3 Traveling wave model

To simulate and analyze the dynamics of the DBR laser we use the traveling wave (TW) model [6]. It governs the temporal-spatial evolution of the complex slowly varying counter-propagating optical fields $E^\pm(z, t)$ (scaled so that $|E|^2 = |E^+|^2 + |E^-|^2$ is the local photon density) and the induced polarization functions $p^\pm(z, t)$:

$$\begin{aligned} \frac{n_g}{c_0} \partial_t E^\pm &= (\mp \partial_z - i\beta(n, I) - \mathcal{D}) E^\pm - i\kappa E^\mp + \mathcal{F}_{sp}^\pm, \\ \text{b.c. : } E^+(0, t) &= r_0 E^-(0, t), \quad E^-(L, t) = r_L E^+(L, t), \\ \mathcal{D} E^\pm &= \frac{\bar{g}}{2} (E^\pm - p^\pm), \quad \partial_t p^\pm = \bar{\gamma} (E^\pm - p^\pm) + i\bar{\omega} p^\pm. \end{aligned} \quad (1)$$

Here, $t \in \mathbb{R}_+$ denotes time, $z \in [0, L]$ corresponds to the longitudinal propagation direction, \mathcal{F}_{sp}^\pm represents the spontaneous emission, r_0 and r_L are the complex field reflectivities at the front and rear facets. The parameters \bar{g} , $\bar{\gamma}$ and $\bar{\omega}$ denote the amplitude, the half width and the peak frequency of Lorentzian approximation of the material gain profile [6], n_g is the group index, and κ is the field coupling coefficient which is different from zero only in the DBR section S_{BG} .

The field equations (1) are coupled to the rate equations for the real excess carrier density $n(z, t)$:

$$\begin{aligned} \partial_t n(z, t) &= \frac{J(z)}{e\sigma} - (An + Bn^2 + Cn^3) - \frac{c_0}{n_g} \Re e \left(\sum_{v=\pm} E^{v*} (g(n) - 2\mathcal{D}) E^v \right), \\ J(z) \Big|_{z \in S_k} &= \frac{I_k}{l_k}, \quad k \in \{A1, A2, BG\}. \end{aligned} \quad (2)$$

Here, $J(z)$ is the injection current density, l_k and I_k are the length and the pump current of the k -th laser section S_k , σ is the cross-section area of the active zone, A , B and C are three coefficients of the cubic nonradiative and radiative spontaneous recombination function. In the presented examples the contacts of the amplifying sections $S_{A1, A2}$ were shortened, so that $J(z) \Big|_{z \in S_{A1, A2}} = I_A / l_A$, where $l = l_{A1} + l_{A2}$ denotes the total length of both amplifier sections.

Table 1: Parameters used in simulations

| | Description | Unit | S_{A1} | S_{A2} | S_{BG} |
|-----------------|-------------------------------|-----------|------------------------|----------|----------|
| l | section length | mm | 2 | 1 | 1 |
| κ | coupling coefficient | $1/cm$ | 0 | | 9.6 |
| J | injection current density | A/cm | [0 – 3] | | 0 |
| $v^{A1,A2}$ | thermal detuning coefficients | nm/A | 0.75 | | 0.2 |
| v^{BG} | | | 0 | | 0 |
| n_g | group refractive index | | 3.6 | | |
| α | internal absorption | $1/cm$ | 2.7 | | |
| δ_s | static detuning | $1/cm$ | –10 | | |
| n_{tr} | transparency carrier density | $1/m^3$ | $1.3 \cdot 10^{24}$ | | |
| n^* | reference carrier density | $1/m^3$ | $0.95 \cdot 10^{24}$ | | |
| g' | effective differential gain | m^2 | $7.26 \cdot 10^{-21}$ | | |
| \tilde{n}' | effective differential index | m^2 | $-7.26 \cdot 10^{-21}$ | | |
| σ | cross-section area of AZ | μm^2 | 0.21 | | |
| A | recombination parameter | $1/ns$ | 0.4 | | |
| B | recombination parameter | m^3/s | $1 \cdot 10^{-16}$ | | |
| C | recombination parameter | m^6/s | $1 \cdot 10^{-41}$ | | |
| \bar{g} | Lorentzian gain amplitude | $1/cm$ | 50 | | |
| $2\bar{\gamma}$ | Lorentzian FWHM | $1/ps$ | 100 | | |
| $\bar{\omega}$ | Lorentzian peak detuning | $1/ps$ | 2 | | |
| λ_0 | central wavelength | μm | 1.064 | | |
| r_0 | front facet reflection | | –0.1 | | |
| r_L | rear facet reflection | | 0.01 | | |

The complex field propagation factor β is defined as

$$\begin{aligned}
 \beta &= \delta(n, I) + \frac{i(g(n) - \alpha)}{2}, \quad \delta = \delta_s + \delta_n(n) + \delta_T(I), \\
 g(n) &= g' n_{tr} \ln \left(\frac{\max\{n, n^*\}}{n_{tr}} \right), \quad \delta_n(n) = \tilde{n}'(n - n_{tr}), \\
 \delta_{T,k}(I) &= \frac{2\pi n_g}{\lambda_0^2} \sum_r v_k^r I_r, \quad r, k \in \{A1, A2, BG\}.
 \end{aligned} \tag{3}$$

Here, the parameters α and δ_s represent the internal absorption and the static detuning. g' and \tilde{n}' are the differentials of the carrier dependent effective logarithmic gain and linear index change functions $g(n)$ and $\delta_n(n)$ at the transparency carrier density n_{tr} . n^* is the reference carrier density for clamping the logarithmic gain function. The coefficients v_k^r of the linear thermal detuning function $\delta_T(I)$ determine the impact of the injection currents I_r to the refractive index change within each laser section S_k [9]. λ_0 , c_0 and e are the central wavelength, the speed of light in vacuum and the electron charge, respectively. The values of the laser parameters used in our simulations are given in Table 1.

4 Mode analysis

Before switching to simulations of the TW model equations (1)-(3) let us discuss the origin of the experimentally observed (see Figs. 2 and 3) periodically reappearing state transitions with the increase of the injection current. For this reason we perform an analysis of the instantaneous optical modes [10] which are determining different continuous wave states observed in experiments.

For any fixed carrier distribution $n(z)$ the optical field equations (1) and the assumption $E(z, t) = \Theta(\beta(n), z)e^{i\Omega(\beta(n))t}$ give rise to the spectral problem

$$\begin{pmatrix} -\partial_z - iD(\beta, \Omega) & -i\kappa \\ -i\kappa & \partial_z - iD(\beta, \Omega) \end{pmatrix} \begin{pmatrix} \Theta^+ \\ \Theta^- \end{pmatrix} = 0, \quad (4)$$

$$\Theta^+(\beta, 0) = r_0 \Theta^-(\beta, 0), \quad \Theta^-(\beta, L) = r_L \Theta^+(\beta, L),$$

$$D(\beta, \Omega) = \beta(n) + \frac{n_g}{c_0} \Omega - \chi(\Omega), \quad \chi(\Omega) = i \frac{\bar{\gamma}}{2} \frac{i(\Omega - \bar{\omega})}{\bar{\gamma} + i(\Omega - \bar{\omega})},$$

where $\chi(\Omega)$ is a frequency (wavelength) dependent contribution of the material gain dispersion.

The *instantaneous*, i.e., carrier dependent optical compound cavity modes are determined by the pairs $[\Theta(z), \Omega]$, where the eigenfunction Θ and the eigenvalue (complex frequency) Ω solve the spectral problem (4). The real and imaginary parts of Ω are the optical angular frequency and the damping of the mode, respectively. Continuous wave (cw) states of the system (1)-(3) are defined by the carrier distribution $\bar{n}(z)$ satisfying balance of the carrier rate equation (2) and the corresponding optical mode $[\Theta(\beta(\bar{n}), z), \Omega(\beta(\bar{n}))]$ with the *real* eigenvalue Ω .

Let us consider some cw state of our TW model determined by functions $\bar{n}(z)$, $\Theta_s(\beta(\bar{n}), z)$ and (real) mode frequency $\Omega_s(\beta(\bar{n}))$. In general, a change of laser parameters (e.g., injection currents) implies some changes of this cw state. Below we present two simple parameter tuning mechanisms preserving carrier and photon distributions $\bar{n}(z)$ and $|\Theta_s(\beta(\bar{n}), z)|^2$ of this state.

The first mechanism can be realized by a uniform change of the propagation factor β in all sections by the same (real) factor $\Delta\beta$. It follows from Eq. (4) that such modification preserves all eigenfunctions $\Theta(\beta, z)$ and shifts the corresponding eigenvalues $\Omega(\beta)$ of the spectral problem (4):¹

$$\Theta(\beta + \Delta\beta, z) = \Theta(\beta, z), \quad \Omega(\beta + \Delta\beta) = \Omega(\beta) - \frac{c_0}{n_g} \Delta\beta.$$

Since the mode frequencies Ω change by a *real* factor, the cw state frequency Ω_s remains real and the (modified) s -th mode $[\Theta_s(z), \Omega_s]$ defines a cw state again. This mode frequency tuning mechanism determines the slow basic red shift $\partial_I \lambda_s$ of the lasing wavelength (see Fig. 3).

¹We neglect small changes of the material gain dispersion for close located frequencies, i.e., assume that $\partial_\xi \chi(\xi)|_{\xi=\Omega} = 0$.

The second mechanism is determined by a shift of the detuning

$$\delta_k \stackrel{def}{=} \frac{1}{l_k} \int_{S_k} \delta(n, I, z) dz$$

in amplifying sections S_{A1} and S_{A2} alone. The field coupling κ in these sections vanishes and the eigenfunctions Θ are given by

$$\Theta^\pm(\beta, z) = \Theta^\pm(\beta, 0) e^{\mp i \int_0^z D(\beta(s), \Omega) ds}, \quad 0 \leq z \leq l_A.$$

The shift of the factor

$$\varphi = 2(l_{A1}\delta_{A1} + l_{A2}\delta_{A2})/2\pi \quad (5)$$

by any integer number m preserves a complex ratio between the mode components Θ^+ and Θ^- at the amplifier/reflector interface $z = l_A$, and, therefore, the distributions $\Theta^\pm(z)$ within the DBR section S_{BG} (up to the multiplier $(-1)^m$). Consequently, an integer shift of the phase factor φ preserves the modal frequencies Ω and the eigenfunction intensity distributions $|\Theta^\pm(z)|^2$. As it will be shown below, such change of φ is responsible for the periodically reappearing lasing mode transitions and for the fast red shift $\partial_I \lambda_f$ of the lasing wavelength.

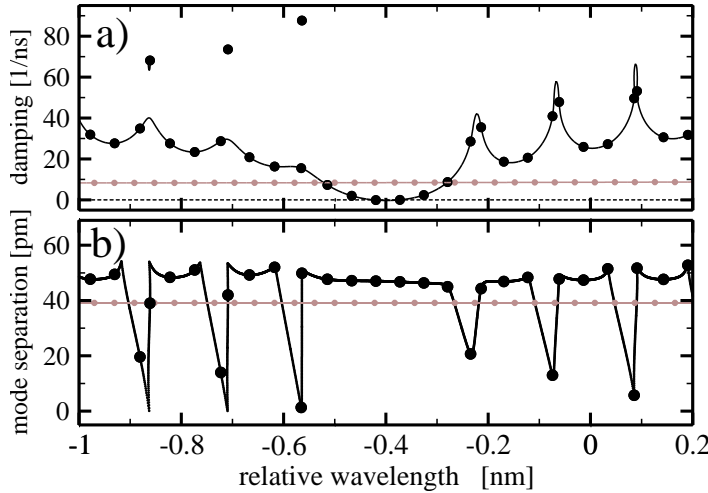


Figure 4: Spectral analysis of the DBR laser (black) and the related Fabry-Perot-type laser (gray). Bullets: complex eigenvalues (a) and wavelength separation of the eigenvalue to its closest blue-wavelength neighbor (b). Curves: changes of the above mentioned quantities with the changing phase factor φ .

To get a deeper understanding of the periodic mode transitions we have performed the mode analysis [10] of the considered DBR laser. The evolution of the complex frequencies Ω computed with some fixed $n(z)$ and tuned phase factor φ is summarized in Figs. 4 and 5. Black bullets in Fig. 4(a) show the location of these eigenvalues in the complex wavelength/damping plain. The black curves connecting these eigenvalues represent their shift with changing φ . The eigenvalues moving along the curve are replacing their next neighbor after a 1-periodic shift of this factor. Note also three separated eigenvalues which move 1-periodic in φ around some small closed loops. These separated loops are implied by the field coupling in the DBR section and can be connected to the main curve or shifted to the large damping values by an appropriate choice of the coupling strength or the field loss parameters.

A mode with the zero damping determines the cw state of the device. The other 5-6 modes located within the stop band of the DBR can be excited by the spontaneous emission noise and, therefore, can be recognized in the optical spectra and the spectral mapping diagrams. To emphasize the mode selection by Bragg grating we consider also the modes of a similar Fabry-Perot (FP) type laser with an increased rear facet reflectivity and a zero coupling factor in the DBR part of the device (see gray bullets and lines in the same diagram).

Another important feature of the DBR section is shown in Fig. 4(b). Here, the black bullets represent the wavelength separation of a mode to its closest blue-wavelength neighbor. In contrast to the FP-type laser (grey bullets and lines) where a ~ 39 pm mode separation is strictly related to the field round-trip time in the device, the mode separation in the DBR laser varies depending on the mode wavelength and the value of the phase factor φ (see the different positions of the black bullets and the variation of the thin black curve). Note, that the separation of the least damped modes at the stop band of the DBR (~ 47 pm in our case) is larger than the mode separation governed by the FP cavity round-trip condition. This is in a nice agreement with the experimentally observed ~ 45 pm mode separation visible in Fig. 3. The increase of the mode separation within the stop-band of the DBR can be explained by the decrease of the effective DBR (and the compound cavity) length for the monochromatic fields with the corresponding optical frequencies.

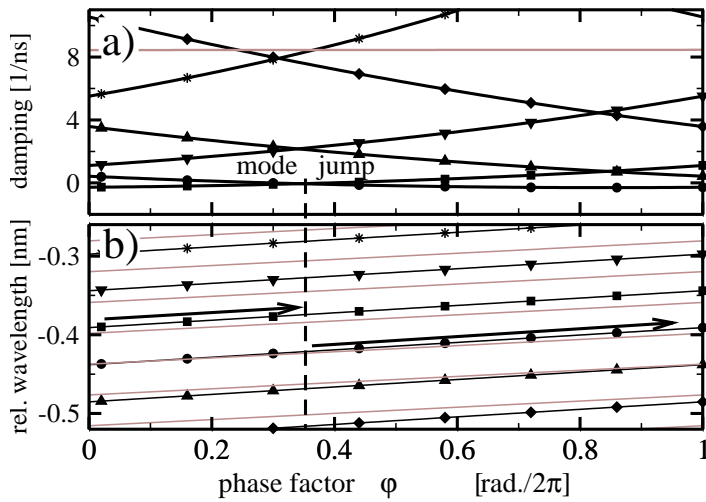


Figure 5: Changes of the damping (a) and the wavelength (b) of several most important modes (indicated by symbols) with the changing phase factor φ . The arrows and the vertical dashed line indicate the dominant modes with the lowest damping and the position where transition between these modes can be expected. Gray lines represent the related Fabry-Perot-type laser.

Fig. 5 gives another representation of the thin curves of Fig. 4. Here we show how the damping (panel a) and the wavelength (panel b) of several most important DBR stop-band modes are changing with the change of the phase parameter φ . Due to periodicity of this parameter, the curves leaving these two diagrams at the right side ($\varphi = 1$) are reentering these diagrams from the left side ($\varphi = 0$).

While the black curves in panel (a) represent only a small change in the main mode

damping, the nearly straight and almost parallel curves in panel (b) suppose an almost linear increase of the modal (and lasing) wavelength with the changing factor φ which is nearly proportional to the injection current into amplifying sections. This linear increase of the modal wavelengths corresponds to the difference between experimentally observed periodically reappearing fast red shift and slow red shift of the lasing wavelengths (see Fig. 3).

The transitions between the modes seen in Fig. 3 occur when the damping of the neighboring mode becomes smaller than the zero damping of the mode determining a cw operation of the laser. A similar situation (even though we assume a fixed in time carrier distribution n) can be recognized in Fig. 5(a). The exchange between the dominant modes represented by bullets and squares is expected close to φ indicated by the vertical dashed line.

The grey lines in Fig. 5 are representing a similar FP-type laser. The damping of the modes is almost independent on the mode number or phase factor φ (see panel a). The mode wavelengths are equidistant and change linearly with the factor φ (see panel b). The mode separation is different from that one of the DBR laser (see discussion above). Consequently, the expected (fast) red shift of the wavelengths in this FP-type laser is smaller than that one of the DBR laser.

Taking into account that the detuning δ changes in all laser sections simultaneously, we conclude:

- The slow red shift of the lasing wavelength

$$\partial_I \lambda_s \approx (\lambda_0^2 / 2\pi n_g) \partial_{I_A} \delta_{BG} \quad (6)$$

observed experimentally occurs due to the changing detuning δ_{BG} .

- The periodicity of the mode transitions with the increasing injection current in the amplifier sections can be approximated by

$$I_{per} = 1 / \partial_{I_A} \tilde{\varphi}, \quad \tilde{\varphi} = \varphi - l_A \delta_{BG} / \pi. \quad (7)$$

The periodic mode transitions occur due to a nearly linear increase of the relative index change function $\tilde{\varphi}$.

- The fast red shift of the lasing wavelength can be approximated by

$$\partial_I \lambda_f \approx \partial_I \lambda_s - \Delta_\lambda / I_{per}, \quad (8)$$

where Δ_λ denotes the wavelength separation between jumping dominant modes.

The mode analysis presented above gives us an explanation of the experimentally observed mode transitions and allows us to estimate some of the coefficients v_k^r entering the thermal detuning model δ_T in Eq. (3). For this reason we estimate the slow wavelength shift $\partial_I \lambda_s$ and the mode transition period I_{per} from Fig. 3, and assume that

the impact of electronic detuning δ_n to the changes of the full detuning δ is small: $\partial_{I_r} \delta_k \approx \partial_{I_r} \delta_{T,k}$. The uniform pumping of both amplifying sections implies

$$\partial_{I_A} \delta_k \approx \frac{v_k^{A1} l_{A1} + v_k^{A2} l_{A2}}{l_A}, \quad k \in \{A1, A2, BG\}.$$

Eqs. (6) and (7) together with the assumptions $v_{A1}^{A1} = v_{A2}^{A2}$ and $v_k^{A1} = v_k^{A2}$ with $k \in \{A1, A2, BG\}$ allow us to fully determine the thermal detuning functions δ_T .

5 Simulations

In this section we present our simulation results and discuss some parameter fitting procedures.

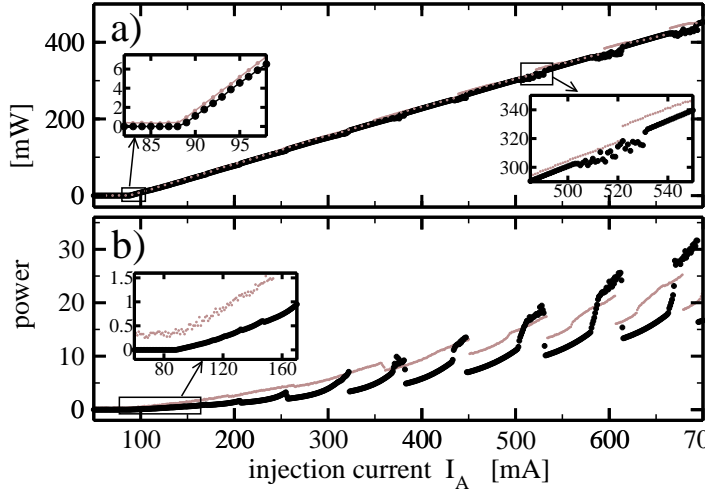


Figure 6: Power-current characteristics of the DBR laser at the front (a) and rear (b) facets. Black: theory. Gray: experiments.

Fig. 6 shows simulated and experimental power-current characteristics of the considered DBR laser. Several basic features such as

- periodically occurring undulations of the emitted power,
- transitions characterized by a sudden increase (decrease) of the power emitted from the front (rear) facets,
- a non-monotonous growth of the power emitted from the rear facet (typical for non-stationary lasing states) before state transitions

are properly reproduced by our simulations. The power increase slopes at both facets of the laser are comparable to experiments and were obtained by a careful choice of the field coupling coefficient κ in the DBR section.

The lasing threshold was fitted mainly by the choice of the logarithmic gain clamping density n^* . Without this factor the modeled field absorption $\alpha - g(n)$ in the un-pumped

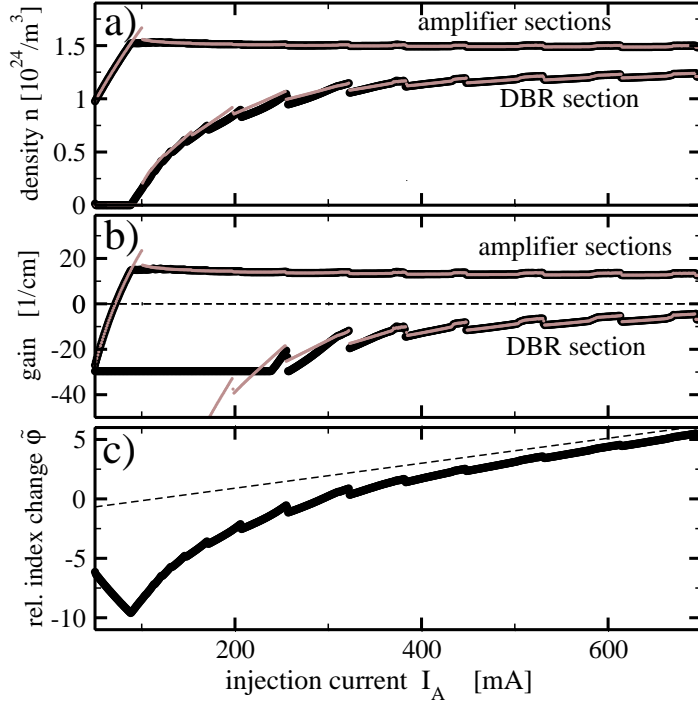


Figure 7: Simulated mean carrier density n (a), gain/loss function $g(n)$ (b) and the relative index change function $\tilde{\varphi}$ from Eq. (7) (c) for increasing injection current I_A . Dashed line in panel (c) is the function $\tilde{\varphi}$ with neglected corrections due to the electronic detuning δ_n . Black and grey: clamped and non-clamped ($n^* = 0$) gain models.

DBR section at the subthreshold regime is un-physically high, what implies an increase of the theoretical threshold current. The difference of these two approaches at small injection currents is illustrated by thick black (clamped model) and thin gray (non-clamped model) dashes in Fig. 7(b). The simulated carrier density values, however, in both these approaches are approximately the same (see panel (a) of the same figure).

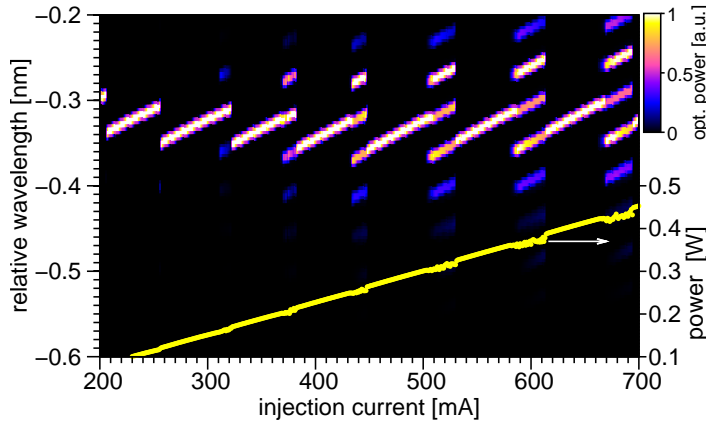


Figure 8: Representation of the simulated optical spectra (mapping) and the emitted power (light curve) at the front facet of the laser as a function of the increased injection current.

Fig. 8 represents an evolution of the simulated optical spectrum with the increase of I_A . Like in experiments (see Fig. 3) we can observe here periodically occurring jumps to a blue neighboring mode in optical spectra, a multiple peak optical spectra before and a single mode emission after the state transitions. The mode separation in simulations is ~ 47 pm, what is comparable to the experiments and is significantly larger than the mode separation in similar FP-type laser. Finally, in both theoretical

and experimental cases the wavelength shift within single “period” of injection current is nearly linear.

Along with similarities Figs. 3 and 8 show us also several discrepancies between simulations and experiments. Comparing to experiments, in simulations we have

- a much more regular periodicity of mode transitions, and
- a less pronounced general slow red shift for larger (> 400 mA) and a blue shift for smaller (< 400 mA) currents.

The first discrepancy is due to our assumption of the *linear* thermal detuning model. Actually, different experimental mode transition periods correspond to different thermal detuning factors ν in Eq. (3).

The second of these effects in our simulations is due to the fast growth of n in DBR section at small super-threshold currents: see the lower black curve in Fig. 7(a). For these injection currents a (blue) electronic shift $\delta_n(n)$ in DBR section plays a significant role. It counteracts and even exceeds the thermal red shift $\delta_T(I)$ in DBR section, what in turn results a general blue wavelength shift visible for small I_A in Fig. 8.

Another effect of this non-vanishing electronic detuning is represented by differences in mode transition period lengths. The derivation of the heating parameters ν from the experimentally estimated slow red shift $\partial_I \lambda_s \approx 20\text{nm/A}$ and the transition period $I_{per} \approx 95$ mA in Section 4 was made by neglecting the contribution of δ_n . For small super-threshold currents electronic detuning $\delta_n(n)$ in the amplifying sections changes only weakly, while in DBR section it decays significantly. This in turn implies an additional positive shift of $\tilde{\varphi}(I)$ which can be even larger than the thermal one: compare slopes of the thin dashed line and thick black curve in Fig. 7(c) representing a pure thermal and a full detuning, respectively. Since modulus 1 change of the function $\tilde{\varphi}(I)$ at lower I_A can be realized much faster than at high I_A , for low injection the mode switchings occur within much shorter current intervals. For increased amplifier currents the intensity of the optical field entering DBR section grows. The balance of the carrier rate equation (2) in this section is kept by increasing the gain (decreasing the loss) function $g(n) < 0$, i.e., by increasing the carrier density which for high injections is slowly approaching the transparency density n_{tr} (see Fig. 7a). Due to a slow change of n at larger currents the contribution of δ_n is by an order smaller than that on of δ_T , and the ≈ 84 mA simulated mode transition period here is only by $\sim 10\%$ smaller than initially assumed one.

This discrepancy could be fixed if forbidding too small carrier densities in DBR section, or assuming some different functional dependence of the index change function δ_n with $\partial_n \delta_n \approx 0$ at small n .

6 Conclusions

We investigated experimentally and numerically the electro-optical behavior of a multi-section DBR semiconductor laser with an active region extending over all sections.

The laser emits an optical power of 600 mW at a current of 900 mA. The power-current characteristics show nearly periodically reappearing jumps, where the power at the front facet increases and the power at the rear facet decreases. With an increase of the injection current the laser device exhibits an averaged slow shift as well as periodically reappearing fast red shifts of the lasing wavelength. The corresponding periodic jumps to adjacent short-wavelength cavity modes are connected with pulsations of the field intensity.

The mode analysis and numerical simulations reveal the mechanisms of the periodic mode jumps, the observed dynamic regimes and the slow or fast shifts of the lasing wavelength. The periodicity of the mode transitions with an increase of injection current is caused by a difference in the refractive index tuning rates in DBR and amplifying sections. The sequence cw operation – mode-beating pulsations – abrupt change of the lasing wavelength is implied by the change of gain and damping of the modes with the change of refractive indices. Here, mode-beating pulsations with a consequent mode jumping are due to the vanishing damping of the neighboring mode which later prevails the previously dominant one.

The averaged slow shift of the lasing wavelength is implied by the dependence of the refractive index in the DBR section on the local carrier density and temperature. At low power the increase of the carrier density due to optical pumping can dominate over the thermal detuning and lead to an average blue shift of the lasing wavelength. At higher power the carrier density in optically well pumped DBR section becomes saturated, what reduces the impact of the electronic detuning with an increase of injection current. The variation of the total detuning in DBR section now is dominated by the increase of the temperature due to cross-heating from the electrically pumped sections, leading to an averaged red shift of the lasing wavelength.

The fast shift is determined by the separation of the neighboring cavity modes, by the length of the mode-transition period and, finally, by the slow wavelength shift rate. By choosing proper dependencies of the refractive index in each section on the currents injected into the same and the other section good agreement between experiment and simulation was obtained.

Acknowledgment

The work of M.R. was supported by DFG Research Center MATHEON “Mathematics for key technologies: Modelling, simulation, and optimization of real-world processes”. H. W. thanks C. Schwanke for support in the numerical simulation.

References

- [1] H. Wenzel, J. Fricke, A. Klehr, A. Knauer, and G. Erbert, "High-Power 980-nm DFB RW Lasers With a Narrow Vertical Far Field," *IEEE Photonics Techn. Lett.*, vol. 18, pp. 737-739, 2006.
- [2] H.K. Nguyen, S. Coleman, N.J. Visovsky, Y. Li, K. Song, R.W. Davis, Jun., M.H. Hu, and C. Zah, "Reliable high-power 1060nm DBR lasers for second-harmonic generation," *Electronics Lett.*, vol. 43, no. 13, pp. 716-717, 2007.
- [3] J. Fricke, H. Wenzel, M. Matalla, A. Klehr, and G. Erbert, "980-nm DBR lasers using higher order gratings defined by i-line lithography," *Semicond. Sci. Technol.*, vol. 20, pp. 1149-1152, 2005.
- [4] R.K. Price, J.J. Borchardt, V.C. Elarde, R.B. Swint, and J.J. Coleman, "Narrow-linewidth asymmetric cladding distributed Bragg reflector semiconductor lasers at 850 nm," *IEEE Photonics Techn. Lett.*, vol. 18, pp. 97-99, 2006.
- [5] M. Achtenhagen, N.V. Amarasinghe, and G.A. Evans: "High-power distributed Bragg reflector lasers operating at 1065 nm," *Electronics Lett.*, vol. 43, pp. 755-757, 2007.
- [6] U. Bandelow, M. Radziunas, J. Sieber, and M. Wolfrum, "Impact of gain dispersion on the spatio-temporal dynamics of multisection lasers," *IEEE J. Quantum Electron.*, vol. 37, pp. 183–188, 2001.
- [7] D. Hofstetter and H. P. Zappe, "Anomalous longitudinal mode hops in GaAs/AlGaAs distributed Bragg," reflector lasers, *Appl. Phys. Lett.*, vol. 710, pp. 181-183, 1997.
- [8] M. Achtenhagen, N. V. Amarasinghe, L. Jiang, J. Threadgill, and P. Young, "Spectral Properties of high-power distributed Bragg reflector lasers," *J. Lightwave Techn.*, vol. 27, pp. 3433-3437, 2009.
- [9] M. Spreemann, M. Lichtner, M. Radziunas, U. Bandelow, H. Wenzel, "Measurement and simulation of distributed- feedback tapered master-oscillator power-amplifiers," *IEEE J. Quantum Electron.*, vol. 45, no. 6, pp. 609–616, 2009.
- [10] M. Radziunas and H.-J. Wünsche, "Multisection Lasers: Longitudinal Modes and their Dynamics," Chapter 5 in *Optoelectronic Devices: advanced simulation and analysis*, ed. J. Piprek, Springer, pp. 121–150, 2005.
- [11] S. Bauer, O. Brox, J. Kreissl, B. Sartorius, M. Radziunas, J. Sieber, H.-J. Wünsche, and F. Henneberger, "Nonlinear dynamics of semiconductor lasers with active optical feedback," *Phys. Rev. E*, vol. 69, p. 016206, 2004.

- [12] M. Radziunas, V.Z. Tronciu, U. Bandelow, M. Lichtner, M. Spreemann, and H. Wenzel, "Mode transitions in distributed-feedback tapered master-oscillator power-amplifier: theory and experiments," *Opt. and Quant. Electron.*, vol. 40, pp. 1103–1109, 2008.
- [13] K.-H. Hasler, B. Sumpf, P. Adamiec, F. Bugge, J. Fricke, P. Ressel, H. Wenzel, G. Erbert, and G. Tränkle, "5-W DBR Tapered Lasers Emitting at 1060 nm With a Narrow Spectral Linewidth and a Nearly Diffraction-Limited Beam Quality," *IEEE Photonics Techn. Lett.*, vol. 20, pp. 1648-1650, 2008.